Impedance Model for Instability Analysis of LCC-HVDCs Considering Transformer Saturation

Qin Jiang, Ruiting Xu, Baohong Li, Xiang Chen, Yue Yin, Tianqi Liu, and Frede Blaabjerg

***Abstract*—In line commutated converter based high-voltage direct current (LCC-HVDC) transmission systems, the transformer saturation can induce harmonic instability, which poses a serious threat to the safe operation of the power system. However, the nonlinear characteristics of the power grids introduced by the transformer saturation considerably limit the application of the conventional analysis methods. To address the issue, this paper derives a linear model for the transformer saturation caused by the DC current due to the converter modulation. Afterwards, the nonlinear characteristics of power grids with the transformer saturation is described by a complex valued impedance matrix. Based on the derived impedance matrix, the system harmonic stability is analyzed and the mechanism of the transformer saturation induced harmonic instability is revealed. Finally, the sensitivity analysis is conducted to find the key factors that influence the system core saturation instability. The proposed impedance model is verified by the electromagnetic transient simulation, and the simulation results corroborate the effectiveness of the proposed impedance model.**

***Index Terms*—Line commutated converter based high voltage direct current (LCC-HVDC), transformer saturation, harmonic instability, impedance model.**

I. Introduction

THE line commutated converter based high-voltage direct current (LCC-HVDC) technologies have been widely used for large-scale and long-distance power transmission [1], [2]. To increase electricity transmission capacity with lower environment impacts, it is common to build high-voltage direct current (HVDC) transmission lines in the existing corridors of high-voltage alternative current (HVAC) transmission lines, like the Hydro-Quebec-New England system [3]-[6].

In the HVAC and HVDC hydro system, the HVAC line may induce the fundamental (1st-harmonic) current on the HVDC line [7], [8]. This coupled fundamental current would then be converted to DC components on the AC side of the converter [9], which consequently causes the transformer saturation and generates positive-sequence 2nd-harmonic current. This 2nd-harmonic component would be modulated back to the DC side as the fundamental component. Therefore, the dynamic interaction between the converter and the transformer saturation may trigger a type of instability, which is called the core saturation instability. For the safe operation of the LCC-HVDC, it is necessary to analyze the core saturation instability [10].

The harmonic instability of the LCC-HVDC has been studied for many years and a typical analysis method is the impedance modeling method [11]. In the impedance analysis, the LCC-HVDC is divided into the line commutated converter (LCC) subsystem and the grid subsystem from the point of common coupling (PCC). The instability of the LCC-HVDC is thus described by the interactivity between a linear system (power grids) and a nonlinear system (LCC), as shown in Fig. 1(a). By linearizing the LCC, the system stability is analyzed. For instance, the sequence-domain impedance models have been developed in [12] and [13] for the LCC to predict the instability of the LCC-HVDC. Considering the phase-locked loop (PLL), the *dq*-frame impedance models are derived for LCC in [14] and [15]. Reference [16] develops a complex *αβ*-frame impedance model from the *dq*-frame impedance model to clearly analyze the frequency coupling effect of the LCC-HVDC. Coupling effects of the characteristic harmonics are taken into consideration with Harmonic state space (HSS) method in [17]-[19]. However, all the above studies only treat the grid side as linear, which may not be the case for the core saturation instability. In practice, the transformer can exhibit a strong nonlinear characteristic under the saturation condition, making the power grids to be nonlinear, as shown in Fig. 1(b). As a result, the conventional methods cannot be applied directly, and the transformer saturation should be taken into consideration for grid impedance modeling.

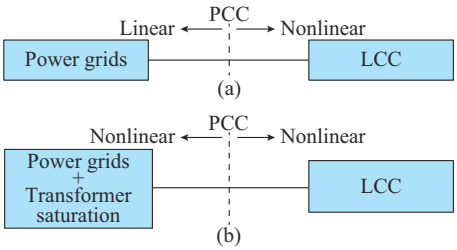

Fig. 1. Interactive system. (a) Without transformer saturation. (b) With transformer saturation.

Manuscript received: May 22, 2023; revised: September 17, 2022; accepted: December 25, 2023. Date of CrossCheck: December 25, 2023. Date of online publication: February 12, 2024.

Q. Jiang, B. Li (corresponding author), X. Chen, Y. Yin, R. Xu, and T. Liu are with the College of Electrical Engineering, Sichuan University, Chengdu 610065, China, and they are also with Smart Grid Key Laboratory of Sichuan Province, Chengdu 610065, China (e-mail: eejqin@scu.edu.cn; scu_lbh@163.com; 349515941@qq.com; yyin2016@126.com; xuruiting@stu.scu.edu.cn; tqliu@scu.edu.cn).

F. Blaabjerg is with the Department of Energy Technology, Aalborg University, Aalborg 9920, Denmark (e-mail: fbl@et.aau.dk).

DOI: 10.35833/MPCE.2023.000340

Although a wide body of research has been reported on the analysis of transformer saturation, mostly focused on the transformer saturation characteristics. In [20], the electrical circuit and the magnetic circuit are combined to predict the distorted excitation current in the saturated transformer. Using the Fourier analysis, [21] and [22] find out that the main component of the excitation current in the single-phase saturated transformer is the 2nd-harmonic. Reference [9] reveals that a three-phase transformer saturated by the converter-modulated DC current can generate positive-sequence 2nd-harmonic current. However, the previous studies lack elaboration of how to incorporate the transformer saturation in the grid impedance modeling process.

The criterion for the core saturation instability of LCC-HVDC has been analyzed in the existing literature. In [9], the circulating loop of the coupled fundamental current in the LCC-HVDC is investigated to explain the mechanism of the instability. A criterion based on the increase of the current in a circulating loop is derived in [9], however, the simulation results show that the criterion is conservative. According to the equivalent impedance change of the system with transformer saturation, a mathematical method is derived to analyze the core saturation instability of the LCC-HVDC in [23]. However, the interaction between the power grids and the converter is not discussed. Reference [11] proposes a frequency-scanning method to assess the core saturation instability of the LCC-HVDC under different operations. It shows that the transformer saturation will induce variations to the power grid impedances, which leads to the core saturation instability. Nonetheless, [11] only provides a rough explanation without any rigorous mathematical analysis. Therefore, it is necessary to provide an accurate and in-depth method to analyze the core saturation instability.

In view of the above gaps, a complex valued impedance modeling method is developed to analyze the core saturation instability of the LCC-HVDC. The main contributions of this paper are summarized as follows.

1) A complex valued impedance model is proposed to describe the nonlinear characteristics of power grids with the transformer saturation. The proposed impedance model can be used to effectively analyze the core saturation instability of LCC-HVDC.

2) The mechanism of core saturation instability for the LCC-HVDC is theoretically and quantitatively explained.

3) The sensitivity study is carried out to find the key factors that affect the core saturation instability of the LCC-HVDC. The results indicate that the knee voltage of the transformer and the impedance of power grids predominantly contribute to the core saturation instability, while the control parameters have very limited impact.

The remainder of this paper is organized as follows. Section II provides the system and variable description. Section III derives the admittance model of the LCC. The impedance model is derived for power grids with the transformer saturation in Section IV. Section V analyzes the system stability and the instability mechanisms. Section VI presents the sensitivity analysis, and Section VII draws conclusions.

II. System and Variable Description

The analysis system is single-pole and 12-pulse, which is constructed by AC system, converter transformer, LCC, and DC transmission line. To simplify the analysis, the receiving end is replaced with an ideal voltage source, but the analysis system contains all the components of a real system, and the derived theory still has migration capabilities.

A. Description of System Under Study

The detail of the analysis system under study is shown in Fig. 2, where i_{dc} and u_{dc} are the current and voltage on the DC line, respectively; u_{coup} is the voltage source employed to imitate the harmonic induced by the parallel AC transmission line; v_{ac} is the voltage at the PCC; u_s is the AC grid voltage; α is the firing angle; $\theta=\omega_1 t$ is the phase angle measured by the PLL, and ω_1 is the fundamental frequency; and R_1-R_3, C_1-C_3, and L_1-L_3 are the resistances, capacitances, and inductances, respectively. The control system is composed of a PLL and a DC-side current control block. The detailed control system is shown in Fig. 3, where k_{pp} and k_{pi} are the control parameters of the PLL; G, T, k_{cp}, and k_{ci} are the control parameters of the DC-side current control; and $i_{dc,ref}$ is the reference value of i_{dc}. As shown in Fig. 2, the system is divided into AC side and converter side from the PCC.

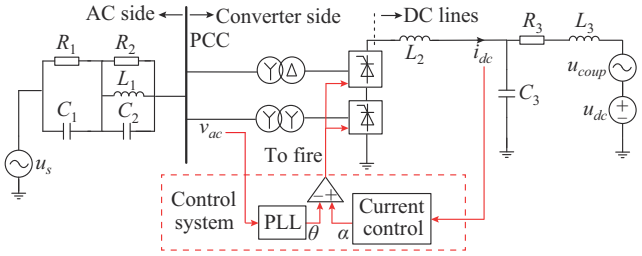

Fig. 2. Detail of analysis system.

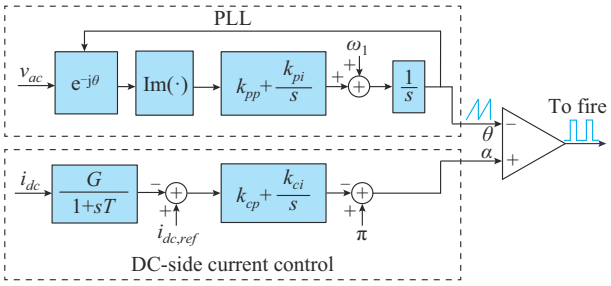

Fig. 3. Control system of LCC-HVDC.

The transfer functions of the control system are expressed as:

$$G_{pll}=\left(k_{pp}+\frac{k_{pi}}{s}\right)\frac{1}{s}\frac{1}{s+\left(k_{pp}+\frac{k_{pi}}{s}\right)\frac{V_d}{s}} \tag{1}$$

$$G_c=\left(k_{cp}+\frac{k_{ci}}{s}\right)\frac{G}{1+sT} \tag{2}$$

where V_d is the magnitude of v_{ac}; G_{pll} is the transfer function of the PLL; and G_c is the transfer function of the DC-side current control.

B. Complex Described Variable

The stationary-frame, i. e., $\alpha\beta$-frame, variables with the subscript "$\alpha\beta$" can be interchangeably represented by the real-space vector and the complex, as shown in (3).

$$\boldsymbol{v}=\begin{bmatrix}v_\alpha\\ v_\beta\end{bmatrix}\leftrightarrow v=v_\alpha+\mathrm{j}v_\beta \tag{3}$$

The dq-frame variables with subscripts "dq" are given as:

$$\boldsymbol{v}_{dq}=\begin{bmatrix}v_d\\ v_q\end{bmatrix}\leftrightarrow v_{dq}=v_d+\mathrm{j}v_q \tag{4}$$

The variables in one reference frame can be transformed to the other as:

$$\boldsymbol{v}_{dq}=\mathrm{e}^{-\mathrm{j}\theta}\boldsymbol{v}\leftrightarrow v_{dq}(s)=v(s+\mathrm{j}\theta) \tag{5}$$

In addition, we have the complex conjugation as:

$$v_{dq}^{*}(s)=v_d(s)-\mathrm{j}v_q(s) \tag{6}$$

III. Admittance Model of LCC

Figure 4 shows the closed-loop diagram of the converter side in Fig. 2, where linearized transfer functions can be calculated according to the linearized modeling method in the previous work [17].

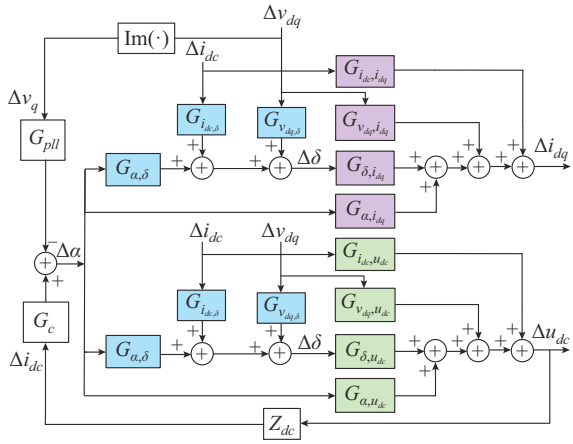

Fig. 4. Closed-loop diagram of converter side.

In Fig. 4, the input small signals are the phase voltage Δv_{dq}, the firing angle $\Delta\alpha$, and the DC current Δi_{dc}. The output signals are the DC-side voltage Δu_{dc} and the AC-side current Δi_{dq}. The extinction delay angle $\Delta\delta$ is employed to describe commutation overlap process of the LCC, which is the sum of $\Delta\alpha$ and the angle of the commutation overlap $\Delta\mu$, i.e., $\Delta\delta=\Delta\alpha+\Delta\mu$. Z_{dc} is the equivalent impedance of the DC lines. $G_{\alpha,u_{dc}}$, $G_{\delta,u_{dc}}$, $G_{i_{dc},u_{dc}}$, and $G_{v_{dq},u_{dc}}$ in the green blocks are the linearized transfer functions between the output Δu_{dc} and the inputs $\Delta\alpha$, $\Delta\delta$, Δi_{dc}, and Δv_{dq}, respectively. The transfer functions in the purple blocks ($G_{\alpha,i_{dq}}$, $G_{\delta,i_{dq}}$, $G_{i_{dc},i_{dq}}$, and $G_{v_{dq},i_{dq}}$) and blue blocks ($G_{\alpha,\delta}$, $G_{i_{dc},\delta}$, and $G_{v_{dq},\delta}$) are defined in the similar way for the output Δi_{dq} and the input $\Delta\delta$, respectively. As an example, the complex transfer function $G_{v_{dq},u_{dc}}$ is expressed as:

$$G_{v_{dq},u_{dc}}=G_{v_d,u_{dc}}+\mathrm{j}G_{v_q,u_{dc}} \tag{7}$$

By rearranging the closed-loop diagram in Fig. 4, the output admittance matrix of the converter side can be calculated, as shown in (8).

$$\begin{bmatrix}I_d(s)\\ I_q(s)\end{bmatrix}=\begin{bmatrix}Y_{dd} & Y_{dq}\\ Y_{qd} & Y_{qq}\end{bmatrix}\begin{bmatrix}V_d(s)\\ V_q(s)\end{bmatrix} \tag{8}$$

where $I_d(s)$ and $I_q(s)$ are the output currents in the dq-frame; $V_d(s)$ and $V_q(s)$ are the input voltages in the dq-frame; and the expressions of Y_{dd}, Y_{dq}, Y_{qd}, and Y_{qq} are given in Appendix A.

The mathematical relationship between the impedance models in the dq-frame and $\alpha\beta$-frame is derived in [17]. Based on this mathematical relationship, the dq-frame admittance in (8) is transformed to the $\alpha\beta$-frame as:

$$\begin{bmatrix}I(s)\\ I^{*}(s-2\mathrm{j}\omega_1)\end{bmatrix}=\begin{bmatrix}Y_s(s-\mathrm{j}\omega_1) & Y_c(s-\mathrm{j}\omega_1)\\ Y_c^{*}(s-\mathrm{j}\omega_1) & Y_s^{*}(s-\mathrm{j}\omega_1)\end{bmatrix}\begin{bmatrix}V(s)\\ V^{*}(s-2\mathrm{j}\omega_1)\end{bmatrix} \tag{9}$$

where $s-2\mathrm{j}\omega_1$ is the coupled frequency of frequency s; and $Y_s(s-\mathrm{j}\omega_1)$ and $Y_c(s-\mathrm{j}\omega_1)$ are the self-admittance and the coupling-admittance, respectively.

In (9), the positive-sequence and negative-sequence variables can be represented by the positive frequency ($s\geq 0$) and negative frequency ($s<0$), respectively. Specifically, the admittances in (9) are calculated as:

$$\begin{cases}Y_s=\dfrac{1}{2}\left[(Y_{dd}+Y_{qq})+\mathrm{j}(Y_{qd}-Y_{dq})\right]\\ Y_s^{*}=\dfrac{1}{2}\left[(Y_{dd}+Y_{qq})-\mathrm{j}(Y_{qd}-Y_{dq})\right]\\ Y_c=\dfrac{1}{2}\left[(Y_{dd}-Y_{qq})+\mathrm{j}(Y_{qd}+Y_{dq})\right]\\ Y_c^{*}=\dfrac{1}{2}\left[(Y_{dd}-Y_{qq})-\mathrm{j}(Y_{qd}+Y_{dq})\right]\end{cases} \tag{10}$$

IV. Impedance Model of Power Grids with Transformer Saturations

When the DC current flows into the transformer, the asymmetrical flux ϕ is induced, as shown in Fig. 5(a). Owing to the nonlinear magnetic characteristics of the transformer in Fig. 5(b), the asymmetrical flux further induces the distorted excitation current i_{exci}, as illustrated in Fig. 5(c).

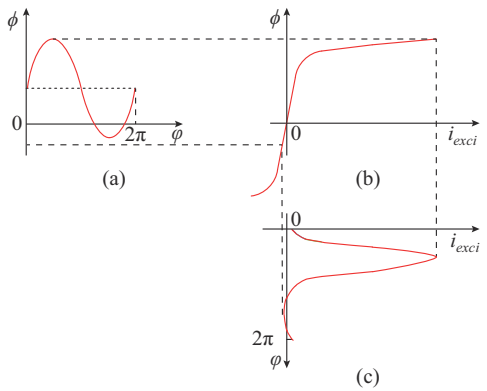

Fig. 5. Excitation current under DC bias. (a) Asymmetrical flux. (b) Nonlinear magnetic curve. (c) Distorted excitation current.

It can be found in [22] that the distorted excitation current is mainly composed of the 2nd-harmonic component. The linear relationship between the amplitude of the 2nd-harmonic excitation current and the input DC current is specified in (11) [9], [23].

$$i_{exci,2}=-ki_{m,0}\cos(2\omega_1 t) \tag{11}$$

where k is the constant saturation coefficient; $i_{exci,2}$ is the 2nd-harmonic current; and $i_{m,0}$ is the input DC current.

Directly influenced by $i_{m,0}$, the 2nd-harmonic components in the three-phase transformer can be calculated using (12).

$$\begin{cases} i_{exci,a,2}=-ki_{m,a,0}\cos 2\omega_1 t \\ i_{exci,b,2}=-ki_{m,b,0}\cos 2\left(\omega_1 t-\dfrac{2\pi}{3}\right) \\ i_{exci,c,2}=-ki_{m,c,0}\cos 2\left(\omega_1 t+\dfrac{2\pi}{3}\right) \end{cases} \tag{12}$$

where the subscripts "abc" represent the three phases.

Based on (12), the linearized model of the three-phase transformer saturated by the converter-modulated DC currents will be derived in Section IV-A. The impedance model of power grids with the transformer saturation will then be presented in Section IV-B.

A. Linearized Relation Between Input DC Current and the 2nd-harmonic Current

According to the modulation theory [12], the coupled fundamental current on the DC transmission line can be modulated into the AC side of the converter as:

$$\begin{cases} i_a=i_1S_{i,a}=I_1\cos(\omega_1 t+\varphi_1)\cdot A_{i,a,1}\cos\omega_1 t \\ i_b=i_1S_{i,b}=I_1\cos(\omega_1 t+\varphi_1)\cdot A_{i,b,1}\cos(\omega_1 t-2\pi/3) \\ i_c=i_1S_{i,c}=I_1\cos(\omega_1 t+\varphi_1)\cdot A_{i,c,1}\cos(\omega_1 t+2\pi/3) \end{cases} \tag{13}$$

where $S_{i,a}$, $S_{i,b}$, and $S_{i,c}$ are the current modulation functions; $A_{i,a,1}$, $A_{i,b,1}$, and $A_{i,c,1}$ are the constant coefficients at the fundamental frequency; φ_1 is the initial phase angle; and I_1 is the amplitude of the coupled fundamental current. Alternatively, (13) can be rewritten as:

$$\begin{cases} i_a=0.5I_1A_{i,a,1}(\cos\varphi_1+\cos(2\omega_1 t+\varphi_1)) \\ i_b=0.5I_1A_{i,b,1}(\cos(\varphi_1+2\pi/3)+\cos(2\omega_1 t+\varphi_1-2\pi/3)) \\ i_c=0.5I_1A_{i,c,1}(\cos(\varphi_1-2\pi/3)+\cos(2\omega_1 t+\varphi_1+2\pi/3)) \end{cases} \tag{14}$$

In (14), the 2nd-harmonic currents flow into the power grids directly, and their effect will be analyzed in the next subsection. In addition, the converter-modulated DC currents in (14) are shown as:

$$\begin{cases} i_{conv,a,dc}=I_{conv,a,dc}\cos\varphi_1 \\ i_{conv,b,dc}=I_{conv,b,dc}\cos(\varphi_1+2\pi/3) \\ i_{conv,c,dc}=I_{conv,c,dc}\cos(\varphi_1-2\pi/3) \end{cases} \tag{15}$$

where $I_{conv,a,dc}$, $I_{conv,b,dc}$, and $I_{conv,c,dc}$ are the amplitudes of the converter-modulated DC currents. Equation (15) shows that the three-phase DC currents are different and their phase angle shifts obey a negative sequence. Therefore, $i_{conv,a,dc}$, $i_{conv,b,dc}$, and $i_{conv,c,dc}$ are called the negative-sequence DC currents in this paper.

Substituting (15) into (12) yields the 2nd-harmonic excitation currents in the three-phase transformer ($i_{trans,a,2}$, $i_{trans,b,2}$, and $i_{trans,c,2}$) under the converter-modulated negative-sequence DC currents:

$$\begin{cases} i_{trans,a,2}=-kI_{conv,a,dc}\cos\varphi_1\cos 2\omega_1 t \\ i_{trans,b,2}=-kI_{conv,b,dc}\cos(\varphi_1+2\pi/3)\cos(2\omega_1 t+2\pi/3) \\ i_{trans,c,2}=-kI_{conv,c,dc}\cos(\varphi_1-2\pi/3)\cos(2\omega_1 t-2\pi/3) \end{cases} \tag{16}$$

Equation (16) can be further rearranged as:

$$\begin{cases} i_{trans,a,2}=-0.5kI_{conv,a,dc}(\cos(2\omega_1 t+\varphi_1)+\cos(2\omega_1 t-\varphi_1)) \\ i_{trans,b,2}=-0.5kI_{conv,b,dc}(\cos(2\omega_1 t+\varphi_1-2\pi/3)+\cos(2\omega_1 t-\varphi_1)) \\ i_{trans,c,2}=-0.5kI_{conv,c,dc}(\cos(2\omega_1 t+\varphi_1+2\pi/3)+\cos(2\omega_1 t-\varphi_1)) \end{cases} \tag{17}$$

The currents $i_{trans,a,2}$, $i_{trans,b,2}$, and $i_{trans,c,2}$ in (17) can be decomposed into zero-sequence and positive-sequence components. The zero-sequence currents that flow into the power grids will induce the zero-sequence voltages $u_{zs,a}$, $u_{zs,b}$, and $u_{zs,c}$ on the AC side of the converter. According to the modulation theory [12], the zero-sequence voltages are then modulated back to the DC side of the converter as:

$$\begin{aligned} u_{dc}=u_{zs,a}S_{u,a}+u_{zs,b}S_{u,b}+u_{zs,c}S_{u,c}= \\ U_{zs}\cos(2\omega_1 t+\varphi_1)\cdot A_{u,a,1}\cos\omega_1 t+ \\ U_{zs}\cos(2\omega_1 t+\varphi_1)\cdot A_{u,b,1}\cos(\omega_1 t-2\pi/3)+ \\ U_{zs}\cos(2\omega_1 t+\varphi_1)\cdot A_{u,c,1}\cos(\omega_1 t+2\pi/3)=0 \end{aligned} \tag{18}$$

where $S_{u,a}$, $S_{u,b}$, and $S_{u,c}$ are the voltage modulation functions of the voltages; $A_{u,a,1}$, $A_{u,b,1}$, and $A_{u,c,1}$ are the fundamental coefficients of the voltage modulation functions; and U_{zs} is the amplitude of the zero-sequence voltage.

Equation (18) indicates that the zero-sequence voltages on the AC side of the converter correspond to zero-sequence voltage after being modulated back to the DC side. This means the zero-sequence currents in (17) cause no interaction between the power grids and the converter. Thus, the zero-sequence currents in (17) can be neglected in the instability analysis. Then, (17) is simplified as:

$$\begin{cases} i_{trans,a,2}=-0.5kI_{conv,a,dc}\cos(2\omega_1 t+\varphi_1) \\ i_{trans,b,2}=-0.5kI_{conv,b,dc}\cos(2\omega_1 t+\varphi_1-2\pi/3) \\ i_{trans,c,2}=-0.5kI_{conv,c,dc}\cos(2\omega_1 t+\varphi_1+2\pi/3) \end{cases} \tag{19}$$

It is clear that $I_{conv,a,dc}$, $I_{conv,b,dc}$, and $I_{conv,c,dc}$ induce the positive-sequence 2nd-harmonic excitation currents in (19). Equation (19) can be transformed into the frequency domain and described by:

$$I_{trans}(s)=-0.5kI^{*}_{conv,dc}(s-2\mathrm{j}\omega_1)\big|_{s=2\mathrm{j}\omega_1} \tag{20}$$

where $I^{*}_{conv,dc}(s-2\mathrm{j}\omega_1)$ is the negative-sequence DC current; and $I_{trans}(s)$ is the 2nd-harmonic component in the excitation current. It is clear that (19) describes the linear relationship between the input DC current and the output 2nd-harmonic current.

B. Impedance Model of Power Grids with Transformer Saturations

In Fig. 6, the transformer is represented as a T equivalent circuit. $I_{conv}(s)$ is the current modulated by the converter; $I_{conv,m}(s)$ and $I_{conv,ac}(s)$ are the parts of $I_{conv}(s)$ that flow into the magnetizing winding and the power grids, respectively;

$V_{conv}(s)$ is the voltage induced by $I_{conv}(s)$; $z_{ac}(s)$ is the impedance of power grids without transformer saturation; $z_{dc}(s)$ is the impedance of the DC transmission line; $\boldsymbol{Y}_{dc}(s)$ is the admittance model of the LCC; L_m and L_c are the magnetizing inductance and the leakage inductance of the transformer, respectively; and $\boldsymbol{Z}_{ac}(s)$ and $\boldsymbol{Z}_{ac+st}(s)$ are defined at the end of this subsection.

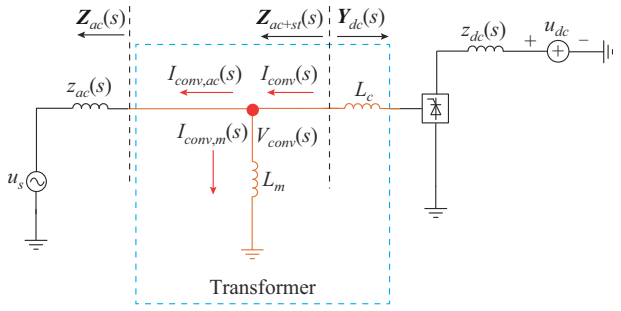

Fig. 6. Current flows in power grids.

With reference to Fig. 6, $I_{conv,ac}(s)$ and $I_{conv,m}(s)$ can be expressed as:

$$I_{conv,ac}(s)=\frac{sL_mI_{conv}(s)}{sL_m+z_{ac}(s)} \tag{21}$$

$$I_{conv,m}(s)=\frac{z_{ac}(s)I_{conv}(s)}{sL_m+z_{ac}(s)} \tag{22}$$

Considering the frequency coupling effect of the converter shown in (9), $I_{conv,ac}(s)$ and $I_{conv,m}(s)$ are extended to the $\alpha\beta$-frame as:

$$\begin{bmatrix} I_{conv,ac}(s) \\ I^*_{conv,ac}(s-2\mathrm{j}\omega_1) \end{bmatrix}=\begin{bmatrix} \dfrac{sL_mI_{conv}(s)}{sL_m+z_{ac}(s)} \\ \left[\dfrac{(s-2\mathrm{j}\omega_1)L_mI_{conv}(s-2\mathrm{j}\omega_1)}{(s-2\mathrm{j}\omega_1)L_m+z_{ac}(s-2\mathrm{j}\omega_1)}\right]^* \end{bmatrix} \tag{23}$$

$$\begin{bmatrix} I_{conv,m}(s) \\ I^*_{conv,m}(s-2\mathrm{j}\omega_1) \end{bmatrix}=\begin{bmatrix} \dfrac{z_{ac}(s)I_{conv}(s)}{sL_m+z_{ac}(s)} \\ \left[\dfrac{z_{ac}(s-2\mathrm{j}\omega_1)I_{conv}(s-2\mathrm{j}\omega_1)}{(s-2\mathrm{j}\omega_1)L_m+z_{ac}(s-2\mathrm{j}\omega_1)}\right]^* \end{bmatrix} \tag{24}$$

Because $sL_m>>z_{ac}(s)$, only the negative-sequence DC current ($I^*_{conv,m}(s-2\mathrm{j}\omega_1)|_{s=2\mathrm{j}\omega_1}$ in (24)) can flow into the magnetizing winding. After substituting (24) into (20), the positive-sequence 2nd-harmonic excitation current $I_{exci,g}(s)$ ($I_{exci,g}(s)=-I_{trans}(s)$) induced by the converter-modulated negative-sequence DC current can be obtained as:

$$\begin{bmatrix} I_{exci,g}(s) \\ I^*_{exci,g}(s-2\mathrm{j}\omega_1) \end{bmatrix}=\begin{bmatrix} \dfrac{k}{2}\left[\dfrac{z_{ac}(s-2\mathrm{j}\omega_1)I_{conv}(s-2\mathrm{j}\omega_1)}{(s-2\mathrm{j}\omega_1)L_m+z_{ac}(s-2\mathrm{j}\omega_1)}\right]^* \\ 0 \end{bmatrix} \tag{25}$$

Given the transformer saturation, the equivalent circuit in Fig. 6 can be changed into Fig. 7. In Fig. 7, the distorted $I_{exci}(s)$ flows into the transformer, while $I_{conv,ac}(s)$ flows out of the transformer. Then, current flowing into the power grids ($I_{ac}(s)$) and inducing the voltage ($V_{ac}(s)$) can be mathematically described as (26). Since $V_{ac}(s)=V_{conv}(s)$ in Fig. 7, (26) can be equivalently written as (27). The matrix $\boldsymbol{Z}_{ac+st}(s)$ in (27) depicts the relationship between the input current and the output voltage of the power grids.

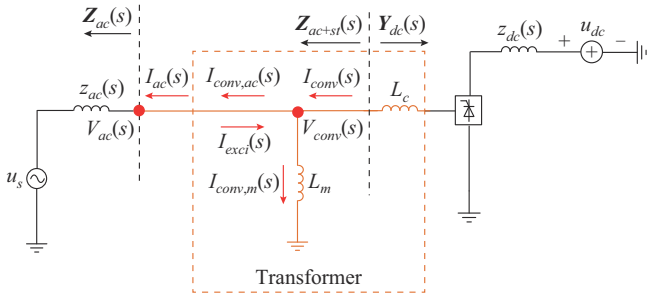

Fig. 7. Current flows in power grids considering 2nd-harmonic excitation current.

$$\begin{bmatrix} V_{ac}(s) \\ V^*_{ac}(s-2\mathrm{j}\omega_1) \end{bmatrix}=\underbrace{\begin{bmatrix} z_{ac}(s) & 0 \\ 0 & z_{ac}(s-\mathrm{j}2\omega_1) \end{bmatrix}}_{\boldsymbol{Z}_{ac}(s)}\cdot \begin{bmatrix} \dfrac{sL_m}{sL_m+z_{ac}(s)}I_{conv}(s)+\dfrac{k}{2}\left[\dfrac{z_{ac}(s-2\mathrm{j}\omega_1)I_{conv}(s-2\mathrm{j}\omega_1)}{(s-2\mathrm{j}\omega_1)L_m+z_{ac}(s-2\mathrm{j}\omega_1)}\right]^* \\ \left[\dfrac{(s-2\mathrm{j}\omega_1)L_mI_{conv}(s-2\mathrm{j}\omega_1)}{(s-2\mathrm{j}\omega_1)L_m+z_{ac}(s-2\mathrm{j}\omega_1)}\right]^* \end{bmatrix} \tag{26}$$

$$\begin{bmatrix} V_{conv}(s) \\ V^*_{conv}(s-2\mathrm{j}\omega_1) \end{bmatrix}=\underbrace{\begin{bmatrix} \dfrac{sL_mz_{ac}(s)}{sL_m+z_{ac}(s)} & \underbrace{\dfrac{k}{2}z_{ac}(s)\left[\dfrac{z_{ac}(s-2\mathrm{j}\omega_1)}{(s-2\mathrm{j}\omega_1)L_m+z_{ac}(s-2\mathrm{j}\omega_1)}\right]^*}_{\text{Coupling impedance}} \\ 0 & \left[\dfrac{(s-2\mathrm{j}\omega_1)L_m}{(s-2\mathrm{j}\omega_1)L_m+z_{ac}(s-2\mathrm{j}\omega_1)}\right]^*z_{ac}(s-2\mathrm{j}\omega_1) \end{bmatrix}}_{\boldsymbol{Z}_{ac+st}(s)}\cdot \begin{bmatrix} I_{conv}(s) \\ I^*_{conv}(s-2\mathrm{j}\omega_1) \end{bmatrix}=\begin{bmatrix} Z_{ac+st,11}(s) & Z_{ac+st,12}(s) \\ 0 & Z_{ac+st,22}(s) \end{bmatrix}\begin{bmatrix} I_{conv}(s) \\ I^*_{conv}(s-2\mathrm{j}\omega_1) \end{bmatrix} \tag{27}$$

Comparing the impedance models of the power grids in (26) and (27), the converter-modulated DC current that flows into the transformer introduces a coupling impedance for the power grids.

V. Simulation Verification

To verify the effectiveness and correctness of the proposed impedance model, the simulation tests are carried out in PSCAD. The system in Fig. 2 is simulated to verify the impedance model of the power grids and the transformer saturation harmonic instability of the LCC-HVDC. The parameters of the LCC-HVDC and the transformer are given in Tables I and II, respectively. In Sections IV-A and IV-B, the derived equivalent admittance models for the LCC-HVDC and power grids with transformer saturation are verified compared with the measured results. In Section IV-C, the correctness of the system harmonic stability analysis method is verified compared with the simulation results.

TABLE I
PARAMETERS OF LCC-HVDC

Parameter	Value	Parameter	Value
u_{dc}	100 kV	K_{ci}	277.8
R_1	10 Ω	K_{pp}	10
R_2	1030 Ω	K_{pi}	50
R_3	1 Ω	G	1
L_1	6.33 mH	i_{dc}	1 kA
L_2	600 mH	u_{coup}	8 kV
L_3	918 mH	V_d	100 kV
C_1	1200 μF	u_s	100 kV
C_2	397.31 μF	T	0.0012 s
C_3	22 μF	R_a, R_b, R_c	0.5 Ω
K_{cp}	0.4540	α	0.28 rad

TABLE II
PARAMETERS OF TRANSFORMER

Parameter	Value
Line-line voltage ratio	100 kV/41 kV
Transformer capacity	80.118 MVA
Leakage reactance	0.13 p.u.
Knee voltage	1.33 p.u.
Magnetizing current	1%

A. Verification of Equivalent Admittance Model for LCC-HVDC

Figures 8 and 9 show the self- and coupling-admittances for the LCC-HVDC under different frequencies, respectively. The calculated results are obtained from (9), while the measured results are obtained via frequency scanning. In Figs. 8 and 9, the calculated results match well with the measured results. Hence, it can be concluded that the admittance model for the LCC-HVDC is accurately derived.

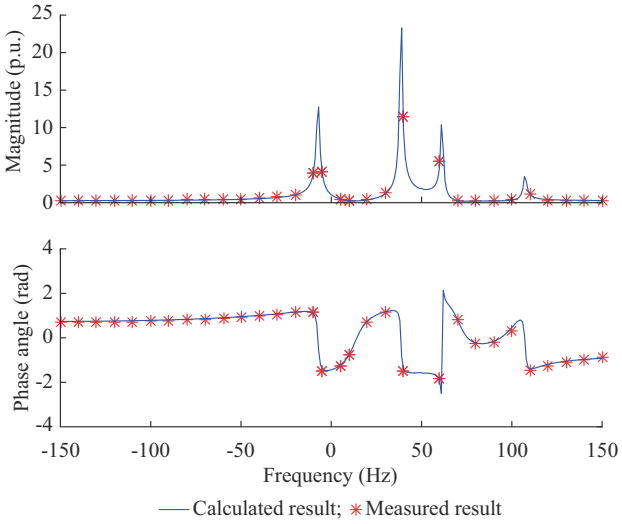

Fig. 8. Frequency response of self-admittance $Y_s(s)$.

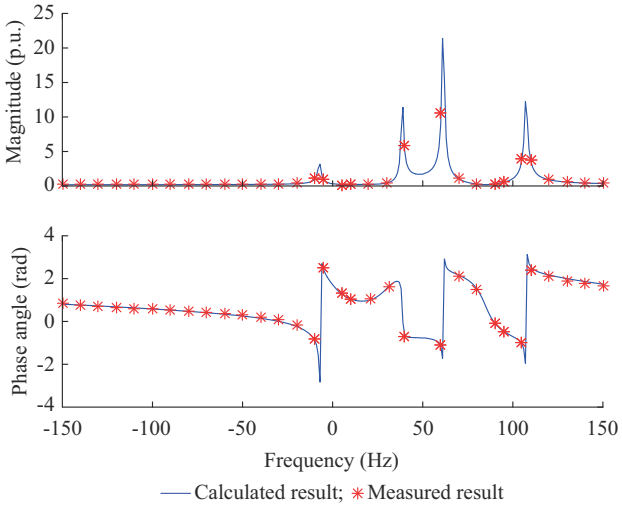

Fig. 9. Frequency response of coupling-admittance $Y_c(s)$.

B. Verification of Impedance Model for Power Grids with Transformer Saturation

As the impedance $Z_{ac+st,22}(s)$ lags only $2j\omega_1$ behind $Z_{ac+st,11}(s)$ in (27), only $Z_{ac+st,11}(s)$ and $Z_{ac+st,12}(s)$ are verified in this subsection. According to Fig. 2, $z_{ac}(s)$ can be calculated as:

$$z_{ac}(s)=R_1 /\!/ \frac{1}{sC_1}+\left(R_2 /\!/ sL_1 /\!/ \frac{1}{sC_2}\right) \tag{28}$$

According to the method in [18], the constant saturation coefficient k in (27) is measured to be 0.5. In Figs. 10 and 11, the calculated results are obtained from (27), while the measured results are obtained based on [17]. The calculated results match well with the measured results in Figs. 10 and 11, which verify the correctness of the proposed impedance model for the power grids with the transformer saturation in (27). In Fig. 11, it can be found that a spike is introduced to $Z_{ac+st,12}(s)$ at 100 Hz owing to the transformer saturation. The value of $Z_{ac+st,11}(s)$ around 0 Hz (highlighted with the green box in Fig. 10) is presented in Fig. 12. It is obvious that $Z_{ac+st,11}(s)$ at 0 Hz is zero owing to the transformer saturation.

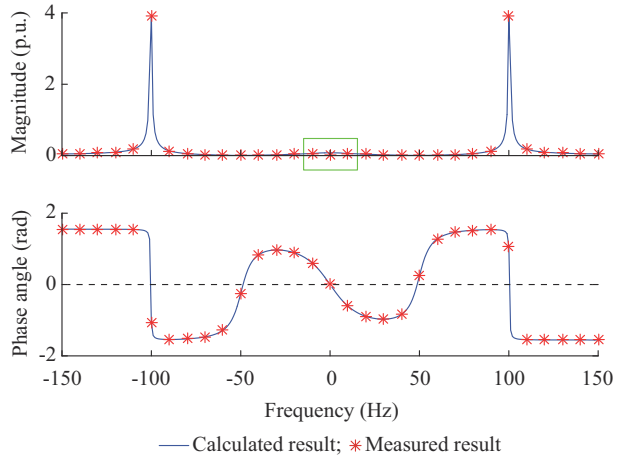

Fig. 10. Frequency response of self-impedance $Z_{ac+st,11}(s)$.

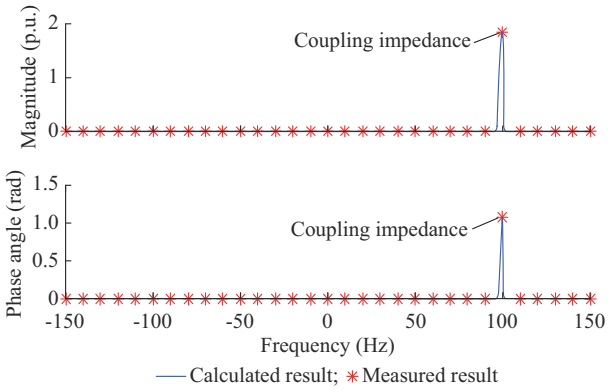

Fig. 11. Frequency response of coupling-impedance $Z_{ac+st,12}(s)$.

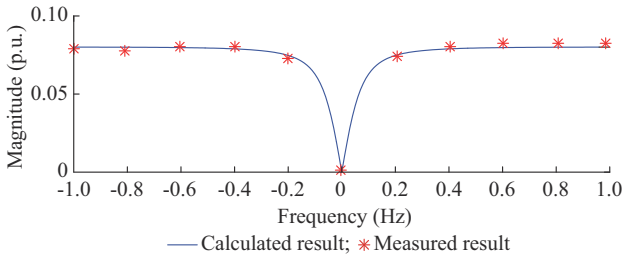

Fig. 12. Frequency response of self-impedance $Z_{ac+st,11}(s)$ around 0 Hz.

C. Stability Analysis and Mechanism of Core Saturation Instability for LCC-HVDC

Utilizing the admittance model for the LCC-HVDC in Section III-A and the impedance model of the power grids in (26) and (27), the Nyquist contours of the LCC-HVDC are drawn according to (29) [24].

$$\det[\lambda \boldsymbol{I}(s) - \boldsymbol{Z}_{ac+st}(s)\boldsymbol{Y}_{dc}(s)] = 0 \tag{29}$$

where $\boldsymbol{I}(s)$ is the unit matrix.

The Nyquist contours when $k = 0.5$ with and without the transformer saturation are shown in Fig. 13. In Fig. 13(a), the brown contour does not encircle the point $(-1, 0)$, which means the system without transformer saturation is stable. However, the blue contour encircles the point $(-1, 0)$. According to the generalized Nyquist stability criterion [24], the system with transformer saturation is predicted to be unstable. According to [9] and [10], the corresponding criterion values with and without transformer saturation are shown in Table III. In Table III, two methods in [9] and [10] predict that the system are unstable whenever the system is with transformer saturation or not.

In Fig. 13(a), the real part of the eigenvalue for the system without transformer saturation is large than -1 at 100 Hz, suggesting the system has positive damping ($-0.01 + 1 > 0$) [12], [24]. However, the real part of the eigenvalue for the system with transformer saturation is less than -1 at 100 Hz, and thus the system has negative damping ($-1.2 + 1 < 0$). The mechanisms of the core saturation instability for the LCC-HVDC can be summarized as follows.

1) The converter-modulated DC current saturates the transformer and induces the positive-sequence 2nd-harmonic current, which is described in (20).

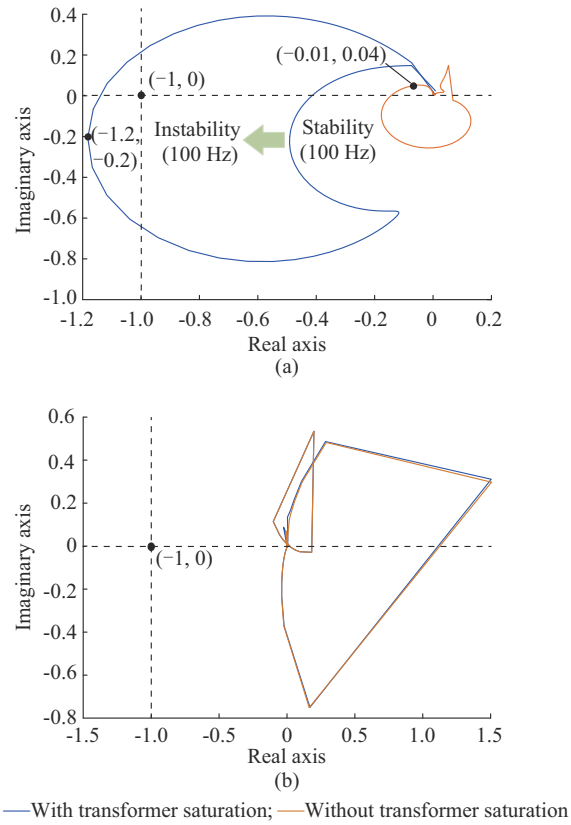

Fig. 13. Nyquist contour when $k = 0.5$. (a) Nyquist contour of the first eigenvalue. (b) Nyquist contour of the second eigenvalue.

TABLE III
CORRESPONDING CRITERION VALUES WITH AND WITHOUT TRANSFORMER SATURATION

Reference	Criterion value	
	With transformer saturation	Without transformer saturation
[9]	−0.6 (unstable)	−1.3 (unstable)
[10]	−0.2 (unstable)	−0.4 (unstable)

2) The induced positive-sequence 2nd-harmonic current changes the equivalent impedance of the power grids, which is described as a coupling impedance shown in (27).

3) According to (29), the coupling impedance degrades the damping of the system from positive to negative, thereby triggering the core saturation instability of the LCC-HVDC.

Based on the model in Fig. 2 and the parameters in Tables I and II, the electromagnetic transient (EMT) simulation is conducted to verify the stability analysis. The fundamental voltage source u_{coup} is set to be 8 kV during the time period of 3.0 - 3.5 s to induce the fundamental current. The measured DC flux of transformer and current on DC transmission line with $k = 0.5$ are shown in Fig. 14.

Before the fundamental voltage is injected, it is clear that the DC flux of the transformer is zero in Fig. 14(a) and the current on the DC transmission line is stable in the Fig. 14(b). After the fundamental voltage is injected, the DC flux rises and does not decay to zero even though the fundamental voltage source is removed at $t = 3.5$ s. As observed from Fig.

14(b), the current on the DC transmission line keeps oscillating after the fundamental voltage source is removed. Therefore, it is concluded that the core saturation instability is triggered, which verifies the prediction results of the proposed impedance model. From Fig. 14, the proposed impedance model is in accordance with the simulation results, which means the proposed impedance model can effectively find core saturation instability of the system. According to Table III, the simulation results show that the methods in [9] and [10] can effectively find the instability of the system with transformer saturation. However, the two criteria cannot effectively find the stability of the system and tend to be conservative when the transformer of the system is not saturated. It can conclude that the proposed impedance model is accurate than those in [9] and [10].

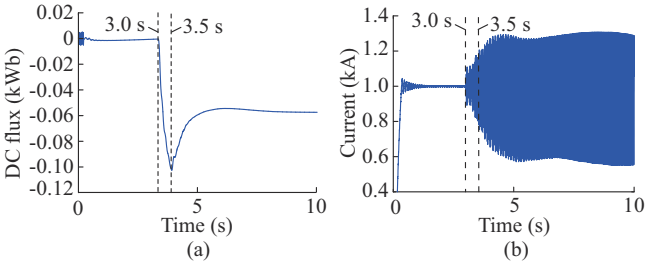

Fig. 14. Measured DC flux of transformer and current on DC transmission line with $k=0.5$. (a) Measured DC flux of transformer. (b) Measured current on DC transmission line.

VI. Sensitivity Analysis

The influences of the knee voltage of transformer, the impedance of power grids, and the control parameters of the LCC-HVDC on the core saturation stability will be analyzed in this section.

A. Sensitivity of Core Saturation Stability to Knee Voltage of Transformer

The knee voltage of transformer is the key factor to decide the saturation coefficient. Thus, the system core saturation stabilities under different knee voltages are analyzed in this subsection. The knee voltages and the corresponding constant saturation coefficients k are shown in Table IV. In addition, the corresponding Nyquist contours are presented in Fig. 15.

TABLE IV
Knee Voltages and Corresponding Constant Saturation Coefficients

Knee voltage (p.u.)	k
1.330	0.500
1.463	0.438
1.490	0.400

In Fig. 15(a), the blue contour ($k=0.5$) encircles the point $(-1,0)$ and the brown contour ($k=0.438$) passes through this point, which means the systems are predicted to be unstable. However, the green contour ($k=0.4$) does not encircle the point $(-1,0)$, thus the system is predicted to be stable. It indicates that the system tends to be stable with a decreased k.

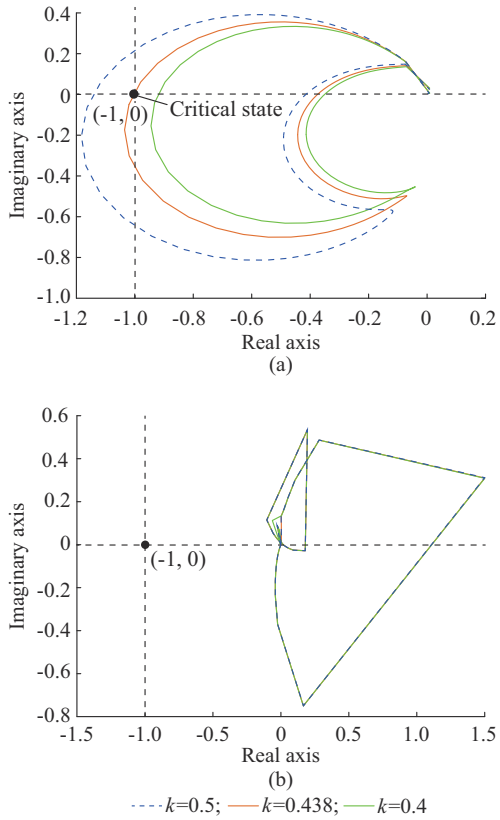

Fig. 15. Nyquist contours with different k. (a) Nyquist contour of the first eigenvalue. (b) Nyquist contour of the second eigenvalue.

The measured current on the DC transmission line with $k=0.438$ and $k=0.4$ are displayed in Fig. 16. Clearly, the system with $k=0.5$ is unstable, which has been verified in Fig. 14. In Fig. 16(a), with $k=0.438$, the current keeps oscillating with a constant amplitude right after the fundamental voltage source is removed at $t=3.5$ s, which demonstrates the system is in critical state. In Fig. 16(b), with $k=0.4$, the oscillating current converges after the fundamental voltage is removed, indicating that the system is stable. The simulation results in Figs. 14 and 16 are in accordance with the predicted results in Fig. 15.

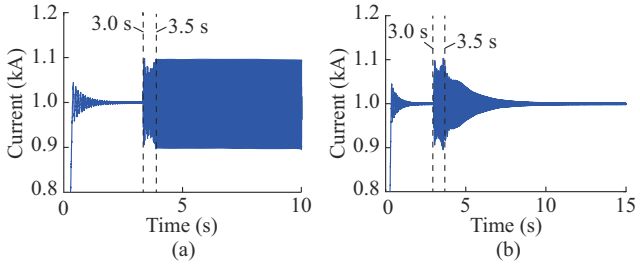

Fig. 16. Measured current on DC transmission line. (a) $k=0.438$. (b) $k=0.4$.

B. Sensitivity of Core Saturation Stability to Impedances of Power Grids

As shown in (27), the impedances of power grids at 100 Hz directly affects the coupling impedance. In this subsec-

tion, the inductance L_1 is changed to analyze its influence on the core saturation stability. The corresponding impedances of power grids at 100 Hz are shown in Table V. As can be observed from Table V, the impedance amplitude of power grids decreases with a reduction in L_1, while the phase angle remains approximately constant. Figure 15 presents the Nyquist contours with different L_1. It is clear from Fig. 17(a) that the blue contour encircles the point (−1, 0) and brown contour passes through that point, which means the system is unstable. In contrast, the green line does not encircle the point (−1, 0), thereby the system is predicted to be stable. From Fig. 17(a), it can be found that the system tends to be stable with a reduction in the impedances of power grids at 100 Hz.

TABLE V
IMPEDANCES OF POWER GRIDS WITH DIFFERENT L_1

L_1 (mH)	Impedance (p.u.)
6.330	3.916∠1.073
6.323	3.489∠1.130
6.310	2.883∠1.210

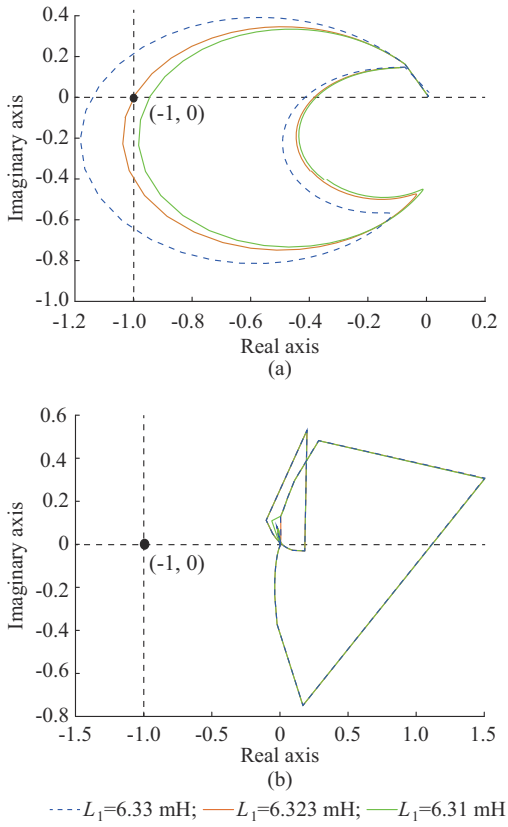

Fig. 17. Nyquist contours with different L_1. (a) Nyquist contour of the first eigenvalue. (b) Nyquist contour of the second eigenvalue.

The measured current on the DC transmission line with different L_1 is shown in Fig. 18. It can be observed that the systems with $L_1 = 6.33$ mH (Fig. 14(b)) and $L_1 = 6.323$ mH (Fig. 18(a)) are unstable, while the system with $L_1 = 6.31$ mH (Fig. 18(b)) is stable. The simulation results are in agreement with the predicted results in Fig. 17. Thus, it can be concluded that the core saturation stability of the LCC-HVDC is improved by reducing the impedance amplitudes of power grids at 100 Hz.

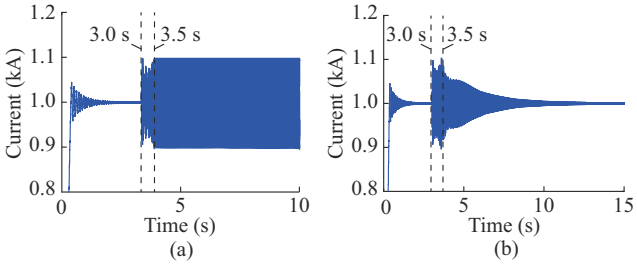

Fig. 18. Measured current on DC transmission line with different L_1. (a) $L_1 = 6.323$ mH. (b) $L_1 = 6.31$ mH.

C. Sensitivity of Core Saturation Stability to Controller Parameter

Equation (29) shows that the DC-side equivalent impedance of the LCC-HVDC can directly influence the stability of the system. Among all the control parameters in Fig. 3, this paper chooses the parameter k_{cp} to shape the impedance of the LCC-HVDC systems. Thus, this subsection investigates the influence of the controller by varying the parameter k_{cp}. The Nyquist contours with different k_{cp} are plotted in Fig. 19.

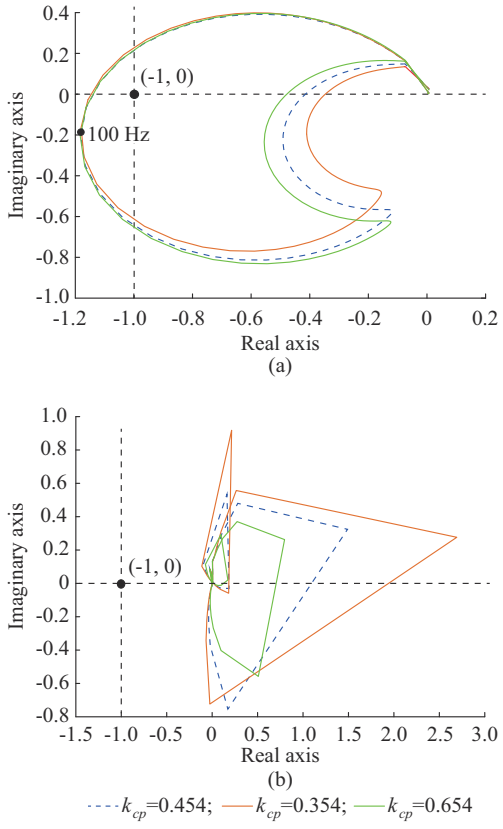

Fig. 19. Nyquist contours with different k_{cp}. (a) Nyquist contour of the first eigenvalue. (b) Nyquist contour of the second eigenvalue.

In Fig. 19(a), the three Nyquist contours encircle point

$(-1, 0)$, which means the system under these three states is unstable. The measured currents on the DC transmission line with different k_{cp} are shown in Fig. 20. It is clear that the system is unstable, which are in accordance with the predicted results in Fig. 19. The simulation results also indicate that the control parameter k_{cp} has a negligible effect on the core saturation instability, and the reasons can be explained as follows.

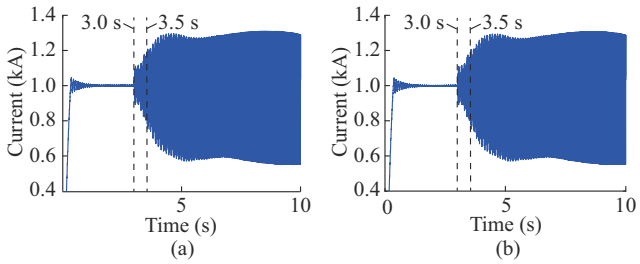

Fig. 20. Measured current on DC transmission line with different k_{cp}. (a) $k_{cp}=0.354$. (b) $k_{cp}=0.654$.

With reference to Fig. 3, the oscillation frequency in the DC-side current control or PLL is equal to the frequency of the DC-side harmonic current (50 Hz) or the q-axis harmonic voltage (50 Hz). The LCC-HVDC employs a fixed duration firing strategy to reduce the harmonic components shown in Fig. 21 [25]. In Fig. 21, only the first firing signal is triggered by the control system in Fig. 3 and the other eleven pulses are sequentially triggered after a fixed duration of π/6 for the twelve-pulse converter. Therefore, there is only one control firing pulse in a fundamental circle and the control frequency for the LCC-HVDC systems is 50 Hz. According to the sampling theorem [26], [27], to rebuild the continuous signal, the frequency of the discrete signal should be twice of the continuous signal at least. It can derive that the LCC-HVDC systems can only effectively generate control signals whose frequency are lower than 25 Hz. Namely, the cut-off frequency for the LCC-HVDC systems is 25 Hz at most, which is lower than the transformer saturation induced oscillation (50 Hz). Therefore, changing the control parameters of the PLL or DC-side current control has little effect on the stability of the system.

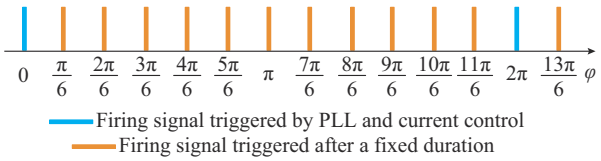

Fig. 21. Firing pulse of LCC-HVDC.

VII. Conclusion

This paper employs the impedance model to analyze the core saturation instability of the LCC-HVDC systems. Through the theoretical analysis and simulation comparisons, the effectiveness of the proposed impedance model is verified.

1) The nonlinear characteristics of the power grids with the transformer saturation can be described by the complex valued impedance matrix, and the impedance model is thus able to analyze the core saturation instability of the LCC-HVDC systems.

2) From the Nyquist-contour-based stability analysis, the results indicate that the transformer saturation degrades the damping of the system from positive to negative by introducing a coupling impedance at 100 Hz. Hence, the core saturation instability can be triggered in the LCC-HVDC systems.

3) The core saturation instability of the LCC-HVDC systems can be enhanced by increasing the knee voltage of the transformer or reducing the impedances of the power grids at 100 Hz. However, the control parameter has little effect on the core saturation instability.

Appendix A

$$\begin{cases} Y_{dd}=G_{v_d,\delta}G_{\delta,i_d}+G_{v_d,i_d}+(G_{\alpha,i_d}G_c+G_{\delta,i_d}G_{i_{dc},\delta}+G_{i_{dc},i_d})(G_{\delta,u_{dc}}G_{v_d,\delta}+ \\ \quad G_{v_d,u_{dc}})/(z_{dc}-G_{i_{dc},u_{dc}}-G_{\delta,u_{dc}}G_{i_{dc},\delta}-G_cG_{\alpha,u_{dc}}) \\ Y_{qd}=G_{v_d,\delta}G_{\delta,i_q}+G_{v_d,i_q}+(G_{\alpha,i_q}G_c+G_{\delta,i_q}G_{i_{dc},\delta}+G_{i_{dc},i_q})(G_{\delta,u_{dc}}G_{v_d,\delta}+ \\ \quad G_{v_d,u_{dc}})/(z_{dc}-G_{i_{dc},u_{dc}}-G_{\delta,u_{dc}}G_{i_{dc},\delta}-G_cG_{\alpha,u_{dc}}) \\ Y_{dq}=G_{v_q,\delta}G_{\delta,i_d}+G_{v_q,i_d}+G_{\alpha,i_d}G_{pll}+(G_{\alpha,i_d}G_c+G_{i_{dc},i_d}+ \\ \quad G_{\delta,i_d}G_{i_{dc},\delta})\dfrac{G_{v_q,u_{dc}}+G_{\delta,u_{dc}}G_{v_q,\delta}-G_{\alpha,u_{dc}}G_{pll}}{z_{dc}-G_{i_{dc},u_{dc}}-G_{\delta,u_{dc}}G_{i_{dc},\delta}-G_cG_{\alpha,u_{dc}}} \\ Y_{qq}=G_{v_q,\delta}G_{\delta,i_q}+G_{v_q,i_q}-G_{\alpha,i_q}G_{pll}+(G_{\alpha,i_q}G_c+G_{\delta,i_q}G_{i_{dc},\delta}+ \\ \quad G_{i_{dc},i_q})\dfrac{G_{\delta,u_{dc}}G_{v_q,\delta}+G_{v_q,u_{dc}}-G_{\alpha,u_{dc}}G_{pll}}{z_{dc}-G_{i_{dc},u_{dc}}-G_{\delta,u_{dc}}G_{i_{dc},\delta}-G_cG_{\alpha,u_{dc}}} \end{cases} \tag{A1}$$

References

[1] Ministry of Water Resource of the People's Republic of China. (2015, Dec.). Water resources development and utilization. [Online]. Available: http://www. mwr. gov. cn/sj/tjgb/szygb/201612/t20161229_783348. html

[2] China Electric Council, "2018–2019 national power supply and demand situation analysis and forecast report," Tech. Rep, Jan. 2020.

[3] Y. Yang, J. Lu, and Y. Lei, "A calculation method for the hybrid electric field under UHVAC and UHVDC transmission lines in the same corridor," *IEEE Transactions on Power Delivery*, vol. 25, no. 2, pp. 1146-1153, Apr. 2010.

[4] G. Wu, C. Yuan, J. Lu *et al*., "Calculation on electromagnetic environment of UHVDC and EHVAC transmission lines erected in a common corridor," *Power System Technology*, vol. 34, no. 2, pp. 14-19, Feb. 2010.

[5] M. Moradi-Sepahvand and T. Amraee, "Hybrid AC/DC transmission expansion planning considering HVAC to HVDC conversion under renewable penetration," *IEEE Transactions on Power Systems*, vol. 36, no. 1, pp. 579-591, Jan. 2021.

[6] J. Qiao, J. Zou, J. Zhang *et al*., "Space-time pattern of ion flow under AC/DC hybrid overhead lines and its application," *IEEE Transactions on Power Delivery*, vol. 33, no. 5, pp. 2226-2235, Oct. 2018.

[7] M. Asif, H. Y. Lee, K. H. Park *et al*., "Influence of placement of overhead ground wires on steady state induction in AC-DC hybrid transmission corridor," *IEEE Transactions on Power Delivery*, vol. 33, no. 6, pp. 2999-3008, Dec. 2018.

[8] H. Ding, Y. Zhang, A. M. Gole *et al*., "Analysis of coupling effects on overhead VSC-HVDC transmission lines from AC lines with shared right of way," *IEEE Transactions on Power Delivery*, vol. 25, no. 4, pp. 2976-2986, Oct. 2010.

[9] S. Chen, A. R. Wood, and J. Arrillaga, "HVDC converter transformer core saturation instability: a frequency domain analysis," *IEE Proceedings-Generation, Transmission and Distribution*, vol. 143, no. 1, pp. 75-81, Jul. 1996.

[10] T. Hasegawa, J. Matsushita, Y. Oue *et al*., "Screening for HVDC system core saturation instability," *IEEE Transactions on Power Delivery*,

vol. 15, no. 4, pp. 1291-1297, Aug. 2000.
[11] J. Sun, "Small-signal methods for AC distributed power systems – a review," *IEEE Transactions on Power Electronics*, vol. 24, no. 11, pp. 2545-2554, Nov. 2009.
[12] M. K. Bakhshizadeh, X. Wang, F. Blaabjerg *et al*., "Couplings in phase domain impedance modeling of grid-connected converters," *IEEE Transactions on Power Electronics*, vol. 31, no. 10, pp. 6792-6796, Oct. 2016.
[13] A. Rygg, M. Molinas, C. Zhang *et al*., "A modified sequence-domain impedance definition and its equivalence to the *dq*-domain impedance definition for the stability analysis of AC power electronic systems," *IEEE Journal of Emerging and Selected Topics in Power Electronics*, vol. 4, no. 4, pp. 1383-1396, Dec. 2016.
[14] X. Ni, A. M. Gole, C. Zhao *et al*., "An improved measure of AC system strength for performance analysis of multi-infeed HVdc systems including VSC and LCC converters," *IEEE Transactions on Power Delivery*, vol. 33, no. 1, pp. 169-178, Feb. 2018.
[15] Y. Qi, H. Zhao, S. Fan *et al*., "Small signal frequency-domain model of a LCC-HVDC converter based on an infinite series-converter approach," *IEEE Transactions on Power Delivery*, vol. 34, no. 1, pp. 95-106, Feb. 2019.
[16] X. Chen, J. Ma, S. Wang *et al*., "An accurate impedance model of line commutated converter with variable commutation overlap," *IEEE Transactions on Power Delivery*, vol. 37, no. 1, pp. 562-572, Feb. 2022.
[17] T. Liu, R. Xu, Q. Jiang *et al*., "Multiple switching functions based HSS model of LCC considering variable commutation angle and harmonic couplings," *IEEE Transactions on Power Delivery*, vol. 38, no. 6, pp. 3820-3833, Dec. 2023.
[18] Y. Liu, X. Zhou, Q. Chen *et al*., "Harmonic state space based impedance modeling and virtual impedance based stability enhancement control for LCC-HVDC systems," *Journal of Modern Power Systems and Clean Energy*, vol. 12, no. 1, pp. 287-298, Jan. 2024.
[19] Y. Wang, F. Xia, Y. Wang *et al*., "Harmonic transfer function based single-input single-output impedance modeling of LCC-HVDC systems," *Journal of Modern Power Systems and Clean Energy*, doi: 10.35833/MPCE.2023.000093.
[20] X. Li, X. Wen, P. N. Markham *et al*., "Analysis of nonlinear characteristics for a three-phase, five-limb transformer under DC bias," *IEEE Transactions on Power Delivery*, vol. 25, no. 4, pp. 2504-2510, Oct. 2010.
[21] X. Zhao, J. Lu, L. Li *et al*., "Analysis of the DC bias phenomenon by the harmonic balance finite-element method," *IEEE Transactions on Power Delivery*, vol. 26, no. 1, pp. 475-485, Jan. 2011.
[22] E. E. Bernabeu, "Single-phase transformer harmonics produced during geomagnetic disturbances: theory, modeling, and monitoring," *IEEE Transactions on Power Delivery*, vol. 30, no. 3, pp. 1323-1330, Jun. 2015.
[23] R. S. Burton, C. F. Fuchshuber, D. A. Woodford *et al*., "Prediction of core saturation instability at an HVDC converter," *IEEE Transactions on Power Delivery*, vol. 11, no. 4, pp. 1961-1969, Oct. 1996.
[24] B. Wen, D. Boroyevich, R. Burgos *et al*., "Small-signal stability analysis of three-phase AC systems in the presence of constant power loads based on measured *d-q* frame impedances," *IEEE Transactions on Power Electronics*, vol. 30, no. 10, pp. 5952-5963, Oct. 2015.
[25] B. Nordstrom, "The three Gorges-Changzhou ±500 kV DC transmission project: Converter Firing Control Technical Report," ABB, China, Tech. Rep, Aug. 17, 2000.
[26] X. Yue, X. Wang, and F. Blaabjerg, "Review of small-signal modeling methods including frequency-coupling dynamics of power converters," *IEEE Transactions on Power Electronics*, vol. 34, no. 4, pp. 3313-3328, Apr. 2019.
[27] J. M. Robert. (2009, Jan.) *Handbook of Fourier Analysis & Its Applications*. [Online]. Available: https://academic.oup.com/book/42033?login=false

Qin Jiang received the B.S. and Ph.D. degrees from the College of Electrical Engineering, Sichuan University, Chengdu, China, in 2016 and 2021, respectively. She was a visiting Ph.D. with the Energy Research Institute, Nanyang Technological University, Singapore, from 2019 to 2020. She is presently a Lecturer with the College of Electrical Engineering, Sichuan University. Her research interests include power system stability analysis and control and high-voltage direct current (HVDC) transmission technologies.

Ruiting Xu received the B.S. degree in electrical engineering from Sichuan University, Chengdu, China, in 2021, where he is currently working toward the Ph. D. degree in electrical engineering. His research interests include HVDC transmission technologies.

Baohong Li received the B.S, M.S., and Ph.D. degrees from the College of Electrical Engineering and Information Technology, Sichuan University, Chengdu, China, in 2009, 2015, and 2018, respectively. From 2009 to 2012, he was with State Grid Corporation of China, Lishui, China. And from September 2019 to September 2020, he has been a Visiting Scholar with Aalborg University, Aalborg, Denmark. He is presently an Associate Professor in the College of Electrical Engineering, Sichuan University. His research interests include power system stability analysis and control, high-voltage direct current transmission technologies, and DC grids.

Xiang Chen received the B.S. and Ph.D. degrees in electrical engineering from Sichuan University, Chengdu, China, in 2014 and 2022, respectively. From 2014 to 2015, he was an Electrical Engineer with State Grid Company, Ltd., Neijiang, China. From December 2018 to April 2020, he was a Guest Ph. D. student with Aalborg University, Aalborg, Denmark. His research interests include the modeling and stability analysis of the power electronic based power systems, and HVDC transmission technology.

Yue Yin received the B.S. degree in School of Mechanical and Energy Engineering from Jimei University, Xiamen, China, in 2006, the M.S. degree in control science and engineering from Sichuan University, Chengdu, China, in 2010, and the Ph.D. degree in electrical engineering from Sichuan University, Chengdu, China, in 2020. She was a visiting Ph.D. student at Stevens Institute of Technology, Hoboken, USA, from 2019 to 2020. She is currently an Associate Professor with the College of Electrical Engineering, Sichuan University. Her research interests include stochastic optimization on power system operation and planning with renewable energy.

Tianqi Liu received the B.S. and M.S. degrees from Sichuan University, Chengdu, China, in 1982 and 1986, respectively, and the Ph.D. degree from Chongqing University, Chongqing, China, in 1996, all are in electrical engineering. Currently, she is a Professor in College of Electrical Engineering and Information Technology at Sichuan University. Her main research interests include power system stability, HVDC, optimal generation dispatch, dynamic security analysis, dynamic state estimation, and load forecast.

Frede Blaabjerg received the Ph.D. degree in electrical engineering from Aalborg University, Aalborg, Denmark, in 1995. From 1987 to 1988, he was with ABB-Scandia, Randers, Denmark. He became an Assistant Professor in 1992, an Associate Professor in 1996, and a Full Professor of power electronics and drives in 1998. In 2017, he became a Villum Investigator. He is honoris causa at University Politehnica Timisoara, Romania, and Tallinn Technical University, Tallinn, Estonia. He was the Editor-in-Chief of the IEEE Transactions on Power Electronics from 2006 to 2012. He was a Distinguished Lecturer for the IEEE Power Electronics Society from 2005 to 2007 and for the IEEE Industry Applications Society from 2010 to 2011 and 2017 to 2018. During 2019-2020, he was the President of IEEE Power Electronics Society. He is currently the Vice-President of the Danish Academy of Technical Sciences too. He was the recipient of 32 IEEE Prize Paper Awards, the IEEE PELS Distinguished Service Award in 2009, the EPE-PEMC Council Award in 2010, the IEEE William E. Newell Power Electronics Award in 2014, the Villum Kann Rasmussen Research Award in 2014, the Global Energy Prize in 2019, and the 2020 IEEE Edison Medal. He was nominated in 2014-2019 by Thomson Reuters to be among the most 250 cited researchers in Engineering in the world. His research interests include power electronics and its applications in wind turbines, photovoltaic (PV) systems, reliability, harmonics, and adjustable speed drives.